Synthesis Mechanism of Cationic Surfactant Templating Mesoporous Silica under an Acidic Synthesis Process

Shunai Che,*,† Huachun Li,† Sunghyun Lim,‡ Yasuhiro Sakamoto,§ Osamu Terasaki,§ and Takashi Tatsumi*,‡,||

Department of Chemistry, School of Chemistry and Chemical Technology, Shanghai Jiao Tong University, 800 Dongchuan Road, Shanghai 200240, People's Republic of China, Structural Chemistry, Arrhenius Laboratory, Stockholm University, S-10691 Stockholm, Sweden, Division of Materials Science & Chemical Engineering, Faculty of Engineering, Yokohama National University, 79-5 Tokiwadai, Yokohama 240-8501, Japan, and CREST, JST, Japan

Received February 17, 2005. Revised Manuscript Received June 16, 2005

The presence of various counteranions in the interfacial region of the silicate−surfactant mesophase introduces opportunities for manipulation of the phase structure. Well-ordered three-dimensional hexagonal $P6_3/mmc$, cubic $Pm\bar{3}n$, two-dimensional hexagonal $p6mm$, and cubic $Ia\bar{3}d$ mesoporous materials have been synthesized with the same surfactant (cetyltriethylammonium bromide), depending on the kind of acids. The counteranions of acidic media have resulted in increasing surfactant packing parameter g in the order $SO_4^{2-} < Cl^- < Br^- < NO_3^-$, which leads to different formation routes to the mesostructures. It has been found that the mesophases are always transformed from the lower curvature one into the higher curvature one in the acidic synthesis gel. The combination of X-ray diffraction patterns, scanning electron microscope images, and high-resolution transmission electron microscope images presented visible evidence for the mesostructural constructions. In particular, the synthesis of a cubic $Pm\bar{3}n$ mesoporous molecular sieve was studied in the presence of trimethylbenzene (TMB) isomers. The rate of transformation is greatly affected by the structure of the TMB isomers and their content; 1,2,3-TMB was the most favorable to the stabilization of the $p6mm$ hexagonal mesophase, 1,3,5-TMB was the least favorable, and 1,2,4-TMB showed intermediate behavior.

Introduction

Since the first discovery of mesoporous materials (FSM-16[1] and M41S families[2]) was made by Yanagisawa et al. and Mobil Research, respectively, other phases such as SBA-*n*,[3] HMS-*n*,[4] KIT-*n*,[5] FDU-*n*,[6] and AMS-*n*[7] have been reported. These mesoporous materials attract a great deal of attention because of their controllable structures and compositions, which make them suitable for wide applications in catalysis, environmental cleanup, and advanced materials design. The understanding of the mechanism relating to surfactant-templated reaction should ultimately lead to a more rational approach to the synthesis of mesoporous materials.

There have been a number of models proposed to explain the formation of mesopores and to provide a rational basis for the various synthesis routes.[8] Huo and co-workers[4b] proposed a generalized liquid crystal templating mechanism based on the specific type of electrostatic interaction between a given inorganic precursor I and a surfactant headgroup S. The basic synthesis route involves the direct co-condensation

* To whom correspondence should be addressed. E-mail: chesa@sjtu.edu.cn (S.C.); ttatsumi@ynu.ac.jp (T.T.).
† Shanghai Jiao Tong University.
‡ Yokohama National University.
§ Stockholm University.
|| CREST.

(1) Yanagisawa, T.; Shimizu, T.; Kuroda, K.; Kato, D. *Bull. Chem. Soc. Jpn.* **1990**, *63*, 988.
(2) (a) Kresge, C. T.; Leonowicz, M. E.; Roth, W. J.; Vartuli, J. C.; Beck, J. S.; *Nature* **1992**, *359*, 710. (b) Beck, J. S.; Vartuli, J. C.; Roth, W. J.; Leonowicz, M. E.; Kresge, C. T.; Schmitt, K. D.; Chu, C. T.-W.; Olson, D. H.; Sheppard, E. W.; McCullen, S. B.; Higgins, J. B.; Schlenker, J. L. *J. Chem. Soc.* **1992**, *114*, 10834.
(3) (a) Huo, Q.; Margolese, D. I.; Ciesla, U.; Feng, P.; Gier, T. E.; Sieger, P.; Leon, R.; Petroff, P. M.; Schüth, F.; Stucky, G. D. *Nature* **1994**, *368*, 317. (b) Huo, Q.; Margolese, D. I.; Ciesla, U.; Demuth, D. G.; Feng, P.; Gier, T. E.; Sieger, P.; Firouzi, A.; Chmelka, B. F.; Schüth, F.; Stucky, G. D. *Chem. Mater.* **1994**, *6*, 1176. (c) Huo, Q.; Leon, R.; Petroff, P. M.; Stucky, G. D. *Science* **1995**, *268*, 1324. (d) Huo, Q.; Margolese, D. I.; Stucky, G. D. *Chem. Mater.* **1996**, *8*, 1147. (e) Zhao, D.; Feng, J.; Huo, Q.; Melosh, N.; Fredrickson, G. H.; Chmelka, B. F.; Stucky, G. D. *Science* **1998**, *279*, 548. (f) Zhao, D.; Huo, Q.; Feng, J.; Chmelka, B. F.; Stucky, G. D. *J. Am. Chem. Soc.* **1998**, *120*, 6024.
(4) (a) Tanev, P. T.; Pinnavaia, T. J. A neutral templating route to mesoporous molecular-sieves. *Science* **1995**, *267*, 865. (b) Bagshaw, S. A.; Prouzet, E.; Pinnavaia, T. J. *Science* **1995**, *269*, 1242.
(5) (a) Ryoo, R.; Kim, J. M.; Ko, C. H.; Shin, C. H. *J. Phys. Chem.* **1996**, *100*, 17718. (b) Kleitz, F.; Choi, S. H.; Ryoo, R. *Chem. Commun.* **2003**, 2136.
(6) (a) Yu, C.; Tian, B.; Fan, J.; Stucky, G. D.; Zhao, D. *J. Am. Chem. Soc.* **2002**, *124*, 4556. (b) Liu, X.; Tian, B.; Yu, C.; Gao, F.; Xie, S.; Tu, B.; Che, R.; Peng, L.; Zhao, D. *Angew. Chem., Int. Ed.* **2002**, *41*, 3876. (c) Yang, H.; Shi, Q.; Liu, X.; Xie, S.; Jiang, D.; Zhang, F.; Yu, C.; Tu, B.; Zhao, D. *Chem. Commun.* **2002**, *23*, 2842. (d) Yu, C.; Tian, B.; Fan, J.; Stucky, G. D.; Zhao, D. *J. Am. Chem. Soc.* **2002**, *124*, 4556.
(7) (a) Che, S.; Garcia-Bennett, A. E.; Yokoi, T.; Sakamoto, K.; Kunieda, H.; Terasaki, O.; Tatsumi, T. *Nat. Mater.* **2003**, *2*, 801. (b) Garcia-Bennett, A. E.; Terasaki, O.; Che, S.; Tatsumi, T. *Chem. Mater.* **2004**, *16*, 813. (c) Che, S.; Liu, Z.; Ohsuna, T.; Sakamoto, K.; Terasaki, O.; Tatsumi, T. *Nature* **2004**, *429*, 281.
(8) (a) Chen, C. Y.; Li, H. Y.; Davis, M. E. *Microporous Mater.* **1993**, *2*, 27. (b) Steel, A.; Carr, S. W.; Anderson, M. W. *J. Chem. Soc. Chem.* **1994**, 1571. (c) Monnier, A.; Schüth, F.; Huo, Q.; Kumar, D.; Margolese, D.; Maxwell, R. S.; Stucky, G. D.; Krishnamurty, M.; Petroff, P.; Firouzi, A.; Janicke, M.; Chemelka, B. F. *Science* **1993**, *261*, 1299. (d) Firouzi, A.; Kumar, D.; Bull, M. L.; Besier, T.; Sieger, P.; Huo, Q.; Walker, S. A.; Zasadzinski, J. A.; Glinka, C.; Nicol, J.; Margolese, D.; Stucky, G. D. *Science* **1995**, *267*, 1138.

10.1021/cm050359s CCC: $30.25
Published on Web 07/15/2005

of anionic inorganic species with a cationic surfactant (S^+I^-); the MCM-41 and MCM-48 are prototypic examples. By operating below the isoelectric point of silica (pH ≈ 2) under acidic conditions, the silica species become cationic (I^+); the silicate mesostructure is formed through the $S^+X^-I^+$ pathway. The ammonium surfactant S^+ is used as a templating agent, but the acid anion X^- becomes involved through this pathway as it serves to buffer the repulsion between the I^+ and S^+ by means of weak hydrogen-bonding forces. In the energetic self-organization it is thought that the packing of the organic surfactant and the charge density matching between the surfactant and the inorganic precursor are essential for the formation of the ordered mesostructure. The surfactant packing depends on the molecular geometry of the surfactant species, such as the number of carbon atoms in the hydrophobic chain, the degree of chain saturation, and the size or charge of the polar headgroup.[3a,9,10] In addition, it has been reported that the formation of mesostructures was affected by the solution conditions, including the surfactant concentration, pH, the presence of cosurfactant, and its concentration and temperature.[11−14]

The acidic route is interesting in that it offers versatile structures and morphologies due to its weaker surfactant/silicate interaction in $S^+X^-I^+$, which suggests that the presence of the counteranion is important for the acidic synthesis systems. However, the effect of the counteranion on the formation of mesostructures in the acidic pathway has remained poorly understood and elusive, largely because of the complicated nature of the multicomponent mixtures, which often required elaborate control of the synthesis conditions and examination of the results. Although it has been shown that counteranions affect the formation of different mesophase structures[3d,12] and mesophase transformation phenomena,[15] it is important in gaining a better understanding of mechanisms of formation to study the effect in a more systematic way.

While the alteration of the structure of cationic moieties of the surfactants has been an effective strategy for controlling the mesophase structure, we have proved that the counteranions produce a dominating effect on the type of mesostructures prepared under different acidic synthesis conditions using various acids. Here we have investigated the influence of additives for the crystallization rate of the mesophase in detail. To observe the structural evolution of the mesophases during synthesis, X-ray diffraction (XRD) patterns of products were measured as a function of the reaction time. The scanning electron microscopy (SEM) and high-resolution transmission electron microscopy (HRTEM) images observation presented visible evidence for the mesostructural transformation.

Experimental Section

Surfactant Preparation. Cetyltriethylammonium bromide (CTEABr) was synthesized by the reaction of cetyl bromide ($C_{16}H_{33}Br$) with triethylamine [$(C_2H_5)_3N$] both from TCI, Japan; $C_{16}H_{33}Br$ (0.5 mol) was added to $(C_2H_5)_3N$ (0.75 mol) in acetone (400 mL). The reaction mixture was stirred for 7 days under reflux conditions. The product was decanted and purified by recrystallization from an acetone solution. The resulting product was separated by filtration and dried under vacuum for several hours at 60 °C.

Synthesis of Mesoporous Materials. Mesoporous materials were synthesized under various conditions using CTEABr as the surfactant, tetraethyl orthosilicate (TEOS; from TCI, Japan) as a silica source, and trimethylbenzenes (TMBs: 1,3,5-TMB, 1,2,4-TMB, and 1,2,3-TMB, from TCI, Japan) as a cosolvent in the presence of various acids: H_3PO_4, H_2SO_4, HF, HCl, HBr, HNO_3, HI, and CH_3COOH. Synthesis was performed as follows: the surfactant, distilled water, cosolvent, and acid were mixed to give a homogeneous solution, which was cooled to 0 °C prior to the addition of TEOS. A desired amount of TEOS precooled to 0 °C was added to the reaction mixture immediately while the mixture was being vigorously stirred. The mixture was stirred for 10 min and then allowed to react at 0 °C under static conditions for desired times. The resultant white precipitates were filtered (without any washing) and dried at 100 °C overnight. Surfactants were removed by calcination in air under static conditions at 600 °C for 6 h.

Characterization. XRD patterns were recorded using an MX Labo powder diffractometer equipped with Cu Kα radiation (40 kV, 20 mA) at the rate of 1.0 deg/min over the range of 1.5−10.0° (2θ). The samples were prepared as thin layers on glass slides.

SEM images were taken using a JXA-8900RL electron probe X-ray microanalyzer. For the SEM observations, the samples were deposited on a sample holder and coated with Pt.

HRTEM images were taken on a JEM-3010 microscope operating at an accelerating voltage of 300 kV. For TEM measurements, all mesoporous materials were crushed in an agate mortar, dispersed in ethanol, and deposited on a microgrid.

N_2 adsorption−desorption isotherms were measured at −196 °C on a Belsorp 28SA sorptionmeter. Samples were pretreated for 2 h at 200 °C and 1.33×10^{-4} Pa. The BET specific surface area, S_{BET}, was calculated using adsorption branches in the relative pressure range from 0.04 to 0.1. The primary mesopore volume V_p was obtained using the high-resolution *t*-plot method. The pore size distribution was calculated from adsorption branches of isotherms using the BJH method, with the corrected Kelvin equation proposed recently.[16]

The CP ^{29}Si NMR spectra were collected at a JEOL-LA400WB 400 MHz spectrometer at 79.4 MHz and a sample spinning frequency of 5 kHz.

(9) Tolbert, S. H.; Landry, C. C.; Stucky, G. D.; Chmelka, B. F.; Norby, P.; Handon, J. C.; Monnier, A. *Chem. Mater.* **2001**, *13*, 2247.
(10) (a) Israelachvili, J. N.; Mitchell, D. J.; Ninham, B. W. *J. Chem. Soc., Faraday Trans. 2* **1976**, *72*, 1525. (b) Israelachvili, J. N.; Mitchell, D. J.; Ninham, B. W. *Biochim. Biophys. Acta* **1977**, *470*, 184. (c) Israelachvili, J. N. *Intermolecular & Surface Forces*; Academic press: London, 1991.
(11) Vartuli, J. C.; Schmitt, K. D.; Kresge, C. T.; Roth, W. J.; Leonowicz, M. E.; McCullen, S. B.; Hellring, S. D.; Beck, J. S.; Schlenker, J. L.; Olson, D. H.; Sheppard, E. W. *Chem. Mater.* **1994**, *6*, 2317.
(12) Kim, M. J.; Ryoo, R. *Chem. Mater.* **1999**, *11*, 487.
(13) Landry, C. C.; Tolbert, S. H.; Gallis, K. W.; Monnier, A.; Stucky, G. D.; Norby, P.; Hanson, J. C. *Chem. Mater.* **2001**, *13*, 1600.
(14) (a) Che, S.; Kamiya, S.; Terasaki, O.; Tatsumi, T. *J. Am. Chem. Soc.* **2001**, *123*, 12089. (b) Che, S.; Lim, S. H.; Kaneda, M.; Yoshitake, H.; Terasaki, O.; Tatsumi, T. *J. Am. Chem. Soc.* **2002**, *124*, 13962. (c) Kamiya, S.; Tanaka, H.; Che, S.; Tatsumi, T.; Terasaki, O. *Solid State Sci.* **2003**, *5*, 197. (d) Lin, H. P.; Kao, C. P.; Mou, C. Y.; Liu, S. B. *J. Phys. Chem. B* **2000**, *104*, 7885.
(15) (a) Xu, J.; Luan, Z.; He, H.; Zhou, W.; Kevan, L. *Chem. Mater.* **1998**, *10*, 3690. (b) Gallis, W. K.; Landry, C. C. *Chem. Mater.* **1997**, *9*, 2035. (c) Cheng, C. F.; Park, D. H.; Klinowski, J. *J. Chem. Soc., Faraday Trans.* **1997**, *93*, 193. (d) Anderson, M. T.; Martin, J. E.; Odinek, J. G.; Newcomer, P. P. *Chem. Mater.* **1998**, *10*, 311. (e) Adam, A. F.; Ruiz, E. J.; Tolbert, S. H. *J. Phys. Chem. B* **2000**, *104*, 5448. (f) Matijasic, A.; Voegtlin, A. C.; Patarin, J.; Guth, J. L.; Huve, L. *Chem. Commun.* **1996**, 1123.
(16) (a) Sayari, A.; Yang, Y.; Kruk, M.; Jaroniec, M. *J. Phys. Chem. B* **1999**, *103*, 3651. (b) Kruk, M.; Jaroniec, M.; Sayari, A. *Langnuir* **1997**, *13*, 6267. (c) Satyari, A.; Liu, P.; Kruk, M.; Jaroniec, M. *Chem. Mater.* **1997**, *9*, 2499.

Elemental analysis was performed on a Perkin-Elmer 2400 Series II CHNS/O analyzer.

Results and Discussions

1. Mesostructure Formation with Different Acids. *1.1. General Trend.* The synthesis of mesoporous silica was performed using TEOS as a silica source and CTEABr as a surfactant under varying acidic conditions with various acids. The synthesis phase diagram (Figure S1, Supporting Information) for the silica−surfactant mesophases obtained in the presence of H_2SO_4, HCl, HBr, and HNO_3 show that long-range organization was established at 0 °C with a surfactant concentration as low as 0.2 wt % for every acid (by weight; as are all reactant concentrations herein). The formation of various mesophases is strongly affected not only by the anions but also by the reactant composition such as the acidity, TEOS/surfactant molar ratio, and anion/surfactant molar ratio of the synthesis gel. The three-dimensional hexagonal $P6_3/mmc$ mesostructures are obtained by using H_2SO_4 and HCl as the acid; H_2SO_4 gives this mesophase in a wider composition range than HCl. The cubic $Pm\bar{3}n$ mesostructures are obtained with three acids: H_2SO_4, HCl, and HBr; HCl gives this mesophase in the widest composition range. The two-dimensional hexagonal *p*6*mm* mesostructure is synthesized in a wide range of reactant compositions when HBr or HNO_3 is used. Only HNO_3 was able to produce the cubic $Ia\bar{3}d$ mesophase among the tested acids, although the range was narrow. It is noteworthy that the phase diagrams are also dependent on the H_2O/Si molar ratio and temperature as well as the synthesis time. For example, the three-dimensional hexagonal $P6_3/mmc$ mesostructures appeared in a wider composition range with decreasing H_2O/Si molar ratio and with increasing temperature in the HCl synthesis system as shown in Figure S2; only the two-dimensional hexagonal *p*6*mm* mesophase appeared in the phase diagram with a longer synthesis time of 4 days in the presence of HNO_3.

1.2. XRD. Figure 1 shows the XRD patterns of as-synthesized mesoporous silica prepared with various acids and compositions at 0 °C for 1 day. The molar composition of the reaction mixture was 0.13:1:*x*:125 CTEABr/TEOS/acid/H_2O, where *x* was varied in the range of 1.0−7.2.

Figure 1a shows the XRD patterns of the materials synthesized with H_2SO_4. The samples synthesized with lower H_2SO_4/CETABr molar ratios in the range of 35−12 show XRD patterns of the three-dimensional hexagonal $P6_3/mmc$ mesophase. The three well-resolved peaks in the range of $2\theta = 1.5-3°$ were indexed to 100, 002, and 101 diffractions, and three additional weak peaks in the range of 3.5−6° were indexed to 110, 103, and 112 diffractions,[14b] which is characteristic of $P6_3/mmc$ three-dimensional hexagonal mesophase with the unit cell parameters $a = 49.473$ Å and $c = 80.978$ Å, for the as-synthesized sample. These give a c/a ratio of 1.637, close to the ideal c/a ratio of 1.633 for the hexagonal close-packed (hcp) structure of hard spheres. The calcined sample also showed a highly resolved XRD pattern with a c/a ratio of 1.639, and the morphology was maintained. The powders from synthesis gels with a higher H_2SO_4/CTEABr molar ratio of 38.5 showed XRD patterns with

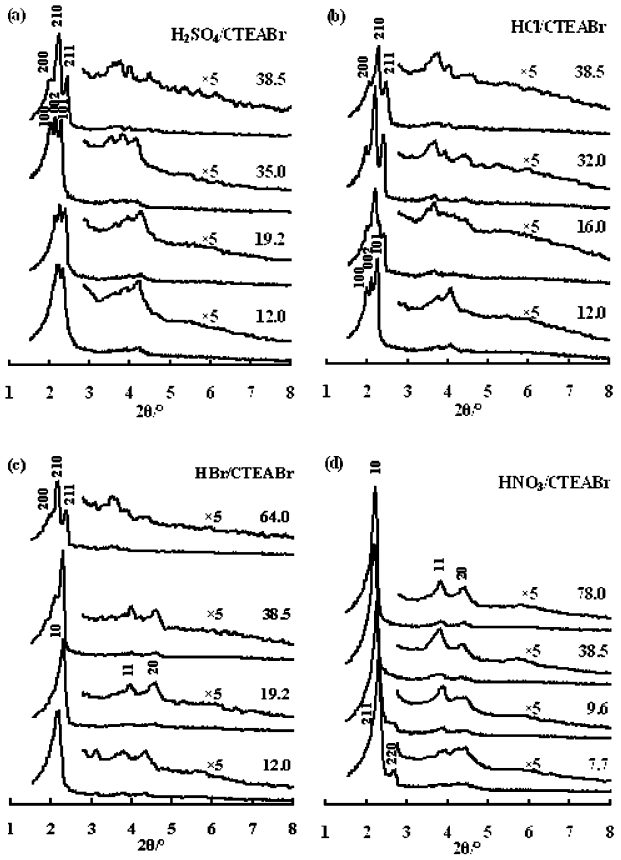

Figure 1. XRD patterns of as-synthesized materials synthesized with various acids at 0 °C for 1 day. Synthesis molar composition: 0.13:1:*x* (inset in each):125 TEOS/CTEABr/acid/H_2O.

three well-resolved peaks in the region of $2\theta = 1.5-3°$, which are indexed to the 200, 210, and 211 diffractions, characteristic of the cubic $Pm\bar{3}n$ mesostructure. Additional weak peaks in the range of 3.5−6°, corresponding to the 220, 310, 222, 320, 321, 400, 411, and 420 reflections, indicate that the as-synthesized materials have a high degree of cubic mesoscopic organization.

In Figure 1b, it can be seen that the three-dimensional hexagonal $P6_3/mmc$ mesophase was synthesized with a lower HCl/CTEABr molar ratio of 12. The mixture of cubic $Pm\bar{3}n$ and three-dimensional hexagonal $P6_3/mmc$ mesophases was synthesized with a HCl/CTEABr molar ratio of 16.0. In a manner similar to the H_2SO_4 system, the cubic $Pm\bar{3}n$ mesophase was obtained with a higher HCl/CTEABr molar ratio of 38.5. With decreasing HCl/CTEABr molar ratios (10.6−7.7), the XRD peak intensities decreased and the lines merged to a single broad peak in the range of $2\theta = 1.5-3°$. It was found that the cubic $Pm\bar{3}n$ mesostructure was dominantly formed in the presence of HCl in a wide composition range.

When the acid HBr was used in the synthesis, the two-dimensional hexagonal *p*6*mm* and cubic $Pm\bar{3}n$ mesophases were formed under the lower and higher HBr/CTEABr molar ratios, respectively (Figure 1c). The sample obtained from a HBr/CTEABr molar ratio of 38.5 proved to be a mixture of the two-dimensional hexagonal *p*6*mm* and cubic $Pm\bar{3}n$ mesophases. The powder from synthesis gels with a lower HBr/CTEABr molar ratio of 19.2 showed XRD patterns with

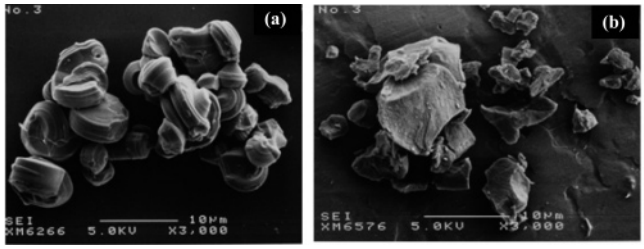

Figure 2. SEM images and surface indexes of the mesoporous materials synthesized with HBr (a) and HNO_3 (b).

one sharp peak in the range of $2\theta = 1.5-3°$ indexed to 10 diffractions and two additional weak peaks in the range of 3.5−6° indexed to 11 and 20 diffractions, which are characteristic of the two-dimensional hexagonal *p*6*mm* mesophase. The formation of $Pm\bar{3}n$ cubic mesophases needed a higher concentrations of acid in the presence of HBr compared to HCl and H_2SO_4, suggesting that HBr favors formation of the two-dimensional hexagonal *p*6*mm* mesophase, which was in agreement with the results obtained by Huo et al. and Kim and Ryoo.[3c,12]

From the XRD patterns presented in Figure 1d, it can be seen that highly ordered mesoporous materials consistent with the cubic $Ia\bar{3}d$ symmetry were obtained with a lower HNO_3/CTEABr molar ratio of 7.7. Two well-resolved 211 and 220 peaks appeared in the 2θ range of 2−3° with *d* spacings of 37.2 and 32.3 Å, and seven weak but resolved 310, 321, 400, 420, 332, 422, and 431 peaks appeared in the 2θ range of 3−6°. On the other hand, the two-dimensional hexagonal *p*6*mm* mesophase was synthesized with a higher HNO_3/CTEABr molar ratio of 19.2. However, only HNO_3 was able to produce the cubic $Ia\bar{3}d$ mesophase among the tested acids.

1.3. SEM and HRTEM. SEM images of as-synthesized samples synthesized with various acids were observed (Supporting Informatin, Figure S3, and Figure 2). All of the three-dimensional hexagonal $P6_3/mmc$ mesophases synthesized with H_2SO_4 and HCl revealed the regular and distinct 20 crystal faces with one six-fold axis (Figure S3a1), which showed high crystallinity as revealed by the XRD patterns. The 20 crystal faces are composed of 2 {100}, 6 {100}, and 12 {101}, which is consistent with 6/*mmm* point group symmetry.

The transmission electron micrograph of the $P6_3/mmc$ crystallite taken in the [100] directions is presented in Figure S4. Obviously, cages are stacked along the *c* axis solely in the "ABAB..." sequence characteristic of the hcp structure. The corresponding electron diffractogram shown in the inset indicates supports extinction conditions of the reflections for the three-dimensional hexagonal symmetry. The image reveals regular periodicity over very large areas, indicating that the crystal is a single crystal of a well-ordered mesostructure. The electron microscopy experiments indicated that the particles are remarkably perfect single crystals.

All of the cubic $Pm\bar{3}n$ mesophases synthesized with higher concentrations of H_2SO_4, HCl, and HBr revealed 54 and 74 regular and distinct crystal faces (or more), which showed high crystallinity as revealed by the XRD patterns. The crystals with 54 and 74 faces had four three-fold axes and exhibited cubic symmetry. The crystal face indexes of the particles having 54 or 74 crystal faces are indicated in Figure S3b1. The 54 crystal faces are composed of 6 {100}, 24 {210}, and 24 {211} planes indexed as shown in Figure S3b2, and the 74 faces are described as 54 face crystals to which 12 elongated hexagons and 8 triangles are added. The elongated hexagons and triangles are {110} and {111} planes in the cubic structure, respectively. The surface patterns with 54 or 74 faces show point group symmetry of $m\bar{3}m$. The mesostrcture and morphology were maintained after calcination with the decreased unit cell parameter from 92.25 to 82.23 Å.

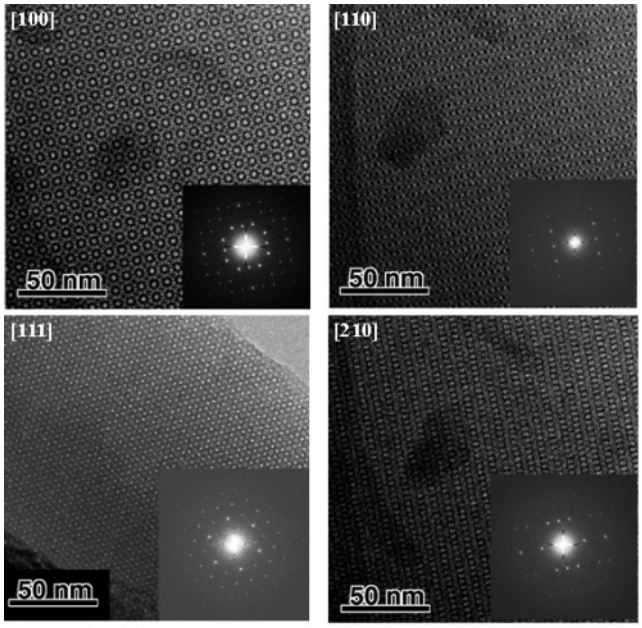

Figure 3. HRTEM images and their Fourier diffractograms of the cubic $Pm\bar{3}n$ mesophase synthesized with HCl.

The sample synthesized with HCl/CTEABr = 32 (molar ratio) was studied by HRTEM. Four transmission electron micrographs of the same crystallite (the [100], [110], [111], and [210] directions) are presented in Figure 3. The corresponding Fourier diffractogram shown in the inset indicates extinction conditions for the reflections. The image revealed regular periodicity over very large areas and clearly indicates that the crystal is a single crystal with a well-ordered mesostructure. The $Pm\bar{3}n$ space group with the same mesostructure was confirmed by an analysis of a set of HRTEM images as previously reported.[17] This is consistent with the results obtained by Sakamoto et al. for particles of single crystals. It can be estimated that all of the samples with the $Pm\bar{3}n$ cubic mesophase XRD patterns and 54 or 74 crystal faces exhibit the same HRTEM images.

The two-dimensional hexagonal *p*6*mm* mesophases synthesized with HBr and HNO_3 show the spiral or gyroid morphology (Figure 2a). These shapes were the morphologies typical of *p*6*mm* two-dimensional hexagonal mesophases.[18] We could not observe regular crystal faces for the materials exhibiting cubic $Ia\bar{3}d$ XRD patterns (Figure 2b).

1.4. N_2 Adsorption−Desorption. All of the calcined samples having high periodicity of the three-dimensional

(17) Sakamoto, Y.; Kaneda, M.; Terasaki, O.; Zhao, D.; Kim, J. M.; Stucky, G. D.; Shin, H. J.; Ryoo, R. *Nature* **2000**, *408*, 449.

hexagonal $P6_3/mmc$, cubic $Pm\bar{3}n$, two-dimensional hexagonal $p6mm$, and cubic $Ia\bar{3}d$ structures as suggested from the XRD patterns show type IV isotherms (Figure S5). All the calcined products synthesized with different acids have BET surface areas larger than 1000 m^2/g, pore volumes greater than 500 mm^3/g, and pore sizes in the range of 26.6−28.3 Å (Supporting Information, Table 2).

The formation of mesoporous structures was strongly influenced by counteranions. The well-ordered mesophases could be readily synthesized from strong acids such as H_2SO_4, HCl, HBr, and HNO_3. The XRD pattern of the material synthesized with H_3PO_4 shows one broad peak, which cannot be indexed to any ordered mesophase. The other acids HF, HI, and CH_3COOH produced an amorphous solid, an opaque gel, and a transparent gel, respectively. Too large and too small counteranions are not able to form the ordered mesophase and to form the disordered or amorphous solid. The weak acids did not have the ability to protonate the silanol group, and we did not observe the formation of mesoporous materials even at a high acid concentration.

1.5. Discussion. As mentioned above, the surfactant and silica are organized by a $S^+X^-I^+$ electronic interaction in the acidic route. In the acidic synthesis process, first, the surfactants form micelles as the combination of the S^+X^- assembly, which, second, form a liquid crystal with molecular silicate species, and finally, the mesoporous material was formed through inorganic polymerization and condensation of the silicate species. In the $S^+X^-I^+$ model, the surfactant-to-counteranion ratio is 1:1 and the H^+ concentration in the solution does not change during the synthesis.

The surfactants with hydrophobic tails and hydrophilic charged headgroups are self-assembled to definite micelle structures. The main controlling forces of these micelle structures involve hydrophobic affinity on the hydrocarbon−water interface and hydrophilic repulsion, ionic repulsion, and steric repulsion of charged headgroups. The surfactant must pack to fill space and, thus, maximize favorable van der Waals interactions between the hydrophobic tails while avoiding high-energy repulsive interactions between the charged or polar headgroups. The packing of the surfactant molecules has been quantified through the use of the packing parameter, $g = V/a_0l$,[3d] where V is the total volume of the hydrophobic chains, a_0 is the effective headgroup area per hydrophilic headgroup, and l is the critical hydrophobic chain length. The a_0 parameter is related to both the size and the charge on the surfactant headgroup and is affected by the electrostatic environment around the surfactant headgroup.

The effect of counteranions on the formation of mesostructures can be explained in terms of the adsorption strength on the headgroups of the surfactant micelle. The X^- ions are more or less hydrated in the surfactant solution. Less strongly hydrated ions have in general smaller ionic radii and bind more strongly on the surface of the surfactant micelles. The adsorption ability or the aggregation number is reported to decrease in the following order: $^1/_2SO_4^{2-} > Cl^- > Br^- > NO_3^-$.[19,20] The well-known binding strength Hofmeister series of anions for the cationic surfactant is increased in the following order of $SO_4^{2-} < Cl^- < Br^- < NO_3^-$.[21] Recent results obtained from direct electromotive force measurement of the degree of the counterion association also follow the above lyotropic order.[22] It is also parallel to the effectiveness of the counterions in decreasing the critical micelle concentration of the cationic surfactant, which is related to the binding affinity and follows the series $SO_4^{2-} < Cl^- < Br^- < NO_3^-$.[23,24]

The counteranion-induced transition of the micelle shape is controlled by the ratio of the size of the polar headgroup to the hydrocarbon part of a surfactant molecule and by the degree of counterion binding on the micelle surface. The first factor is related to the geometrical packing of the anion between the polar headgroups. As mentioned above, the hydrated radii of anions is decreased in the order of $^1/_2SO_4^{2-} > Cl^- > Br^- > NO_3^-$. The second factor is related to the electrostatic repulsion among polar headgroups. The counteranion binding on the micelle surface may be affected by the counteranion species and/or the concentration of acid or salt added. It has been considered that the existence of the ion opposite to the surfactant headgroups would decrease the repulsion that efficiently decreases the a_0 value. The affinity of anions on the surface headgroup would increase in the following order: $SO_4^{2-} < Cl^- < Br^- < NO_3^-$. On the basis of the radii and affinity order, it is reasonable that among the four acids H_2SO_4 led to the formation of the smallest g parameter mesophase, and that HNO_3 was favorable for the formation of the larger g parameter mesophase. Although the initially formed mesophases were the same for the H_2SO_4 and HCl synthesis systems, the formation of higher curvature three-dimensional hexagonal $P6_3/mmc$ mesophases was easier in the presence of H_2SO_4 compared to HCl, which corresponds to the larger size of anion SO_4^{2-}. Therefore, the g parameter value of the formed mesophase was increased in the following order: $SO_4^{2-} < Cl^- < Br^- < NO_3^-$. The larger the hydrated radii, the stronger the affinity and the more reduced the repulsion of headgroups, which leads to decreased a_0 and increased g parameter values of micelles.

From the synthesis-space diagram of mesophase structures, it can be seen that the higher and lower curvature mesophases appear in the upper and lower parts of the synthesis-phase diagram, respectively, in the presence of H_2SO_4 or HCl and vice versa in the presence of HBr or HNO_3. The formation of mesophases is controlled both thermodynamically and kinetically. It is generally recognized that the lower the surfactant concentration,[11] the higher Si/surfactant[3d] and

(18) (a) Ozin, G. A.; Yang, H.; Sokolov, I.; Coombs, N. *Adv. Mater*. **1997**, *9*, 662. (b) Khushalani, D.; Kuperman, A.; Ozin, G. A.; Tanaka, K.; Garcés, J.; Olken, M. M.; Coombs, N. *Adv. Mater.* **1995**, *7*, 842.

(19) Schick, M. J. *J. Colloid Sci.* **1962**, *17*, 801.
(20) Ray, A.; Nemethy, G. *J. Am. Chem. Soc.* **1971**, *93*, 6787.
(21) Rubingh, D. N.; Holland, P. M. *Cationic surfactant: Physical Chemistry*; Surfactant Science Series 37; Marcel Dekker: New York, 1991.
(22) Gaillon, L.; Lelievere, J.; Gaboriaud, R. *J. Colloid Interface. Sci.* **1999**, *213*, 287.
(23) (a) Gamboa, C.; Ríos, H.; Sepúlveda, L. *J. Phys. Chem.* **1989**, *93*, 5540. (b) Tanford, C. *The Hydrophobic Effect: Formation of Micelles and Biological Membranes*; Wiley: New York, 1973.
(24) (a) Ozeki, S.; Ikeda, S. *J. Colloid Interface. Sci.* **1980**, *77*, 219. (b) Ozeki, S.; Ikeda, S. *J. Colloid Interface. Sci*. **1982**, *87*, 424.

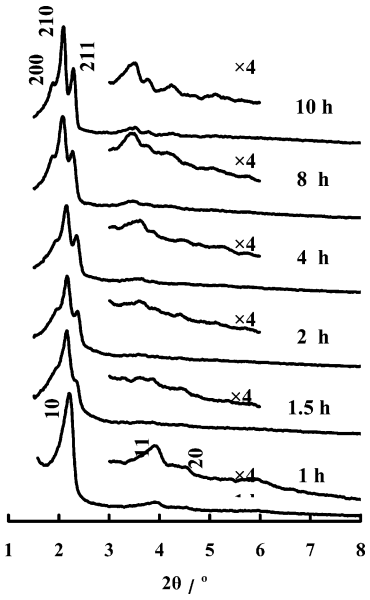

Figure 4. XRD patterns of as-synthesized materials synthesized without any addition of cosolvent at 0 °C for various times. Synthesis molar composition: 1:0.13:5:125 TEOS/CTEABr/HCl/H_2O.

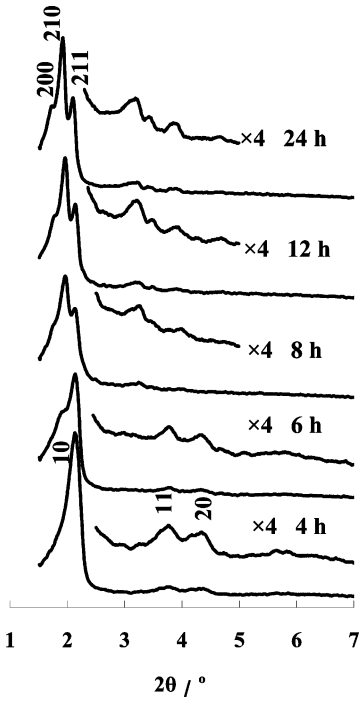

Figure 5. XRD patterns of as-synthesized materials synthesized by the addition of 1,3,5-TMB at 0 °C for various times. Synthesis molar composition: 1:0.13:5:125:0.13 TEOS/CTEABr/HCl/H_2O/1,3,5-TMB.

higher surfactant/counteranion ratio favor[23] the formation of higher curvature mesophases thermodynamically. Therefore, the composition of the lower parts of the diagram should favor the formation of higher curvature mesophases. However, in the case of HBr and HNO_3, the counteranion is so small that the transition of the mesophase is not governed by the thermodynamic factor; furthermore, the condensation rates are so slow that mesophase creation is more kinetically controlled, leading to the results different from those obtained for H_2SO_4 and HCl. It has been well-known that the concentration of [H^+] influences strongly the condensation reaction of silicate species. Silica condensation causes the positive charge density of the silicate network to decrease. It can be considered that the organic surfactants pack to form a high surface curvature to adjust the effective headgroup area maintaining charge matching in the interface so that the higher curvature mesophases are formed under higher acidity conditions.

2. Time Course of Phase Transformation. *2.1. Phase Transformation Behavior with and without Addition of TMB Isomers.* To observe the structural evolution of the mesophases during synthesis, XRD patterns and SEM and HRTEM images of the products were obtained as a function of the reaction time.

Figures 4, 5, S6, and S7 show the XRD patterns obtained with a composite synthesized in the $Pm\bar{3}n$ mesostructure at an HCl/CTEABr molar ratio of 25.0. The samples were produced without any addition of cosolvent (Figure 4) and with addition of 1,3,5-TMB (Figure 5), 1,2,4-TMB (Figure S6) and 1,2,3-TMB (Figure S7), respectively. The mesophases originating from the same initial mixture except for the organic additives were sampled at different reaction times between 1 and 24 h.

In the absence of the organic additive (Figure 4), the material sampled at 1 h showed the three peaks 10, 11, and 20 based on the hexagonal symmetry with a d_{100} spacing of 3.8 nm, and only after 1.5 h three peaks 200, 210, and 211 due to the cubic phase started to appear and the hexagonal peak was decreased. The cubic peaks continue growing with time; after 24 h, a highly ordered cubic mesostructure with a_0 of 8.8 nm was formed. It is interesting to note that the 10 reflection of the hexagonal mesophase was transformed smoothly into the 211 reflection of the cubic mesophase, which suggests a geometric correlation between the (10) planes of the hexagonal mesophase and the (211) planes of the cubic mesophase. The particles were gradually transformed from irregular to spherical shape; the characteristic cubic phase morphology with 54 crystal faces starts to appear after 12 h of reaction time (not shown).

In a manner similar to the synthesis without addition of cosolvent, the hexagonal mesophase with a d_{100} spacing of 4.1 nm was formed at first and converted to the cubic mesophase with a_0 of 10.3 nm when the synthesis was conducted with the addition of 1,3,5-TMB/CTEABr = 1.0 (Figure 5). However, it is noteworthy that the mesophase transformation rate was slowed with addition of the cosolvent. The hexagonal mesophase remained even after 4 h of reaction time, and when the synthesis was conducted for 5−10 h three peaks in the range of $2\theta = 1.5-3.5°$ started to appear at the expense of the hexagonal phase peaks, which cannot be indexed to any mesophase, however. It might be estimated that these samples consisted of two types of mesophases. After 12 h the 11 and 20 peaks of the two-dimensional hexagonal phase disappeared and many new peaks appeared simultaneously in the range of $2\theta = 3.5-6°$. All the new peaks gradually sharpened and increased in intensity with time. The three peaks of the samples obtained after 12−24 h were indexed to a set of cubic phase peaks 200, 210, and 211, indicating that the hexagonal mesophase was formed at first, and converted to the cubic $Pm\bar{3}n$ mesophase through the intermediate mixture state. It has been

found that the hexagonal phase was finally transformed to the cubic phase even at the 1,3,5-TMB/CTEABr ratio of 4.0.

The changes in XRD patterns for as-synthesized materials sampled at different times from the synthesis gels with 1,2,4-TMB/CTEABr molar ratios of 0.5 and 1.0 are shown in parts a and b of Figure S6, respectively. The behavior of synthesis with 1,2,4-TMB/CTEABr = 0.5 was similar to that of the synthesis with 1,3,5-TMB/CTEABr = 1.0. In contrast to the above observations, it is important to note that the two-dimensional hexagonal was not transformed to the cubic phase even after 4 days for the synthesis with 1,2,4-TMB/CTEABr = 1.0 added, indicating that 1,2,4-TMB is favorable to the stabilization of the hexagonal phase compared to 1,3,5-TMB.

Figure S7 shows the XRD patterns of as-synthesized samples produced with 1,2,3-TMB/CTEABr = 0.3 (a) and 0.5 (b), respectively. The behavior of synthesis with 1,2,3-TMB/CTEABr = 0.3 and 0.5 were similar to the synthesis with 1,2,4-TMB/CTEABr = 0.5 and 1.0, respectively. The materials sampled at 4 h (sample denoted here by T4) with 1,2,3-TMB/CTEABr = 0.3 (Figure S7a) showed the three peaks 10, 11, and 20 based on the hexagonal system with a d_{100} spacing of 3.8 nm, and the materials sampled between 5 and 9 h (T5−T9) show the unindexable peaks. After 8 h the 11 and 20 peaks disappeared and three peaks in the range of $2\theta = 1.5-3.5°$ of the samples obtained after 8−24 h (T8−T24) were indexed to a set of cubic phase peaks 200, 210, and 211. The unit cell parameter of the sample T24 was 9.5 nm. It can be seen that the 10 reflection of the hexagonal mesophase was also transformed to the 211 reflection of the cubic mesophase. As will be discussed later, the samples T4, T12, and T24 were confirmed to show *p*6*mm* and $Pm\bar{3}n$ phases, respectively, by electron microscopy observations. In contrast, the hexagonal mesophase was not transformed to the cubic mesophase even after 4 days for the synthesis with only 1,2,3-TMB/CTEABr = 0.5 added, indicating that 1,2,3-TMB strongly prevents the construction of the cubic mesophase. It is interesting to note that the irregular morphology that appeared at the early stage was transformed to the spiral and gyroid shapes, which is typical hexagonal mesophase morphology, for the samples synthesized with 1,2,3-TMB/CTEABr = 0.5 (not shown). Thus, the effect of stabilizing the hexagonal *p*6*mm* phase was increased in the following order: 1,3,5-TMB < 1,2,4-TMB < 1,2,3-TMB.

To observe the behavior of the surfactant in the micelle during the mesophase transformation, we have measured the Si-based yields, surfactant-based yields, and Si/CTEABr molar ratios of products in the synthesis system with addition of 1,2,3-TMB/CTEABr = 0.3. The silica yield and the surfactant-based yield were increased with time (not shown), and the Si/CTEABr molar ratio of the product was also increased with time as shown in Figure S8. The increase in the Si/CTEABr ratio indicates the decrease in the amount of charge-balancing CTEA cation against silica, suggesting that the charge density of the silica wall is decreased with time and concomitant increase in the silica yield.

Figure 6 shows the ^{29}Si MAS NMR data of the samples with 1,2,3-TMB/CTEABr = 0.3 molar ratio, which were used to determine the degree of polymerization and the concentration of silanol groups, as measured by the ratio Q_3/Q_4. All the spectra of the samples T2, T4, and T10 show three major peaks Q_2 (90 to 91 ppm), Q_3 (−101 to 102 ppm), and Q_4 (−110 to −111 ppm). The Q_3 peaks of all the samples were substantially intense compared to Q_4 peaks, indicating a low condensation degree of the silicate species, which enables the phase transformation. The Q_3/Q_4 ratios of the three samples were decreased with the reaction time, reflecting progressive silanol condensation during the formation of the cubic mesophase. This result may suggest that the driving force of the phase transformation from hexagonal to cubic phase is the progress of silica polymerization.

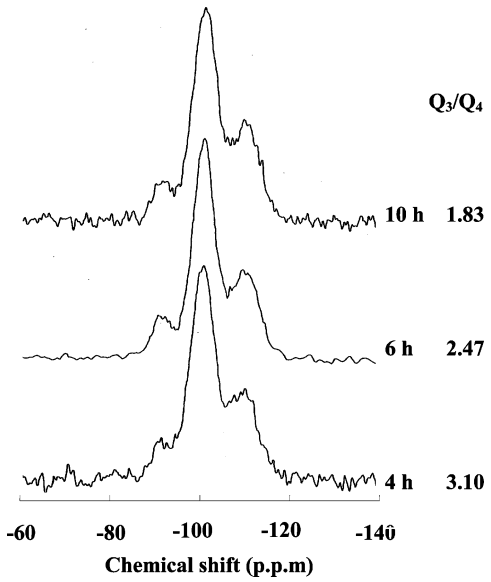

Figure 6. ^{29}Si MAS NMR spectra of as-synthesized materials synthesized by the addition of 1,2,3-TMB at 0 °C for various times.

As mentioned above, the cubic $Pm\bar{3}n$ mesophase was formed through the phase transformation during the synthesis, and the rate of the transformation was affected by the addition of organic species to the reaction mixture including inorganic species. The inorganic and organic arrays of the mesostructure should meet at the interface. The interface curvature is energetically determined so as to optimize charge repulsion and van der Waals interactions.

Phase transition can be explained by the surfactant packing parameter *g*. Small values of *g* favor a phase with more curved surfaces such as $Pm\bar{3}n$ ($g < 1/3$) and *p*6*mm* ($g = 1/2$), while large values favor structures with smaller curvature such as $Ia\bar{3}d$ ($1/2 < g < 2/3$) and *p*2 layers ($g = 1$).[3d] Phase transition between the above phases are associated with changes in the curvature of the interface and may be understood phenomenologically as a competition between the elastic energy of bending the interfaces and energies resulting from the constraints of interfacial and charge separation. It has been reported that the transformation from the lamellar phase to the cubic MCM-48 phase was caused by the decrease in the packing parameter through silica condensation.[8c,15a]

In the cubic $Pm\bar{3}n$ mesophase synthesis system, first, the hexagonal *p*6*mm* mesophase with higher *g* parameter ($g = 1/2$) was formed, which was transformed to the cubic phase with lower *g* parameter ($g = 1/3$). The driving force for this

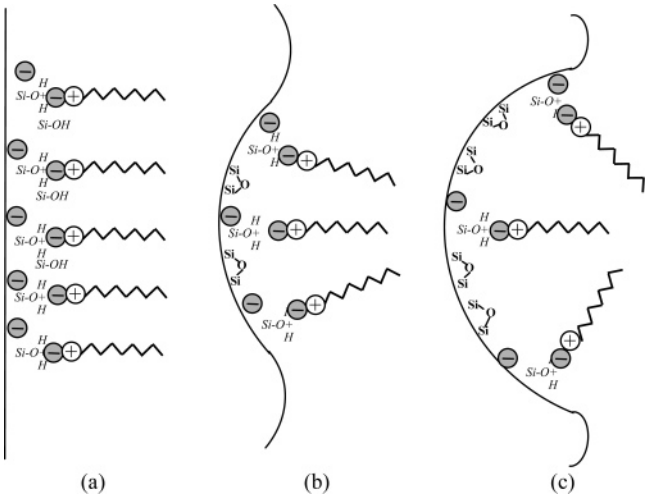

Figure 7. Schematic presentation of the curvature changes according to the charge density that occurs in the silica−surfactant interface during the phase transformation. (a) Lower curvature hexagonal structure, (b) intermediate state between hexagonal and cubic structure, (c) higher curvature cubic structure.

phase transformation from a hexagonal to a cubic mesophase seems to be polymerization of silica species during the synthesis. Silica condensation causes the positive charge density of the silicate network to decrease. As shown in Figure 7, the silica framework is positively charged in the acidic synthesis condition. The positive charge is balanced with the positive charge on the surfactant with intermediation of counteranion. When silicate condensation proceeds, the protonated alkoxide groups produce siloxane bonds and as a result the charge density decreased as shown in Figure S8. To maintain charge matching in the interface, the organic surfactants pack to form a high surface curvature to increase the effective headgroup area and lower the packing parameter so that the cubic mosophases with higher *g* parameters are favored. The silica condensation was indicated by the ^{29}Si NMR, which shows the decrease in the Q_3/Q_4 ratio during the transformation. Generally, it is considered that ethanol produced from TEOS hydrolysis tends to reside primarily in the outer shell of a surfactant micelle, which increases the effective surfactant volume *V* in the interface, raising the value of packing parameter *g*. For example, the MCM-41 mesophase with lower *g* parameter can be transformed to the MCM-48 mesophase with higher *g* parameter with progress in TEOS hydrolysis.[15] In our case, the production of ethanol does not seems to be very important in this transformation, because the hydrolysis of TEOS is so rapid that the migration of ethanol was completed before the phase transformation.

First, an apolar symmetric compound 1,3,5-TMB tends to be associated with the hydrophobic part of the surfactant micelle. The penetration of the cosolvent molecules increases the hydrophobic volume, raising the value of the packing parameter *g* and, thus, requiring a longer time for the phase transformation.

The transformation behavior is quite sensitive to a subtle difference in the structure among the TMB isomers. It is conceivable that one-side-substituted 1,2,3-TMB can enter the hydrophobic−hydrophilic "palisade" region of the micelle, with a relatively large increase in the volume of the hydrophobic core to form surfactant molecule aggregates with a lower curvature surface. For the 1,2,3-TMB/CTEABr = 0.5 system, the driving force of silica polymerization might not be sufficient to decrease the effective *g* parameter value to cause the transformation to the $Pm\bar{3}n$ phase. It can be considered that the structure of 1,2,4-TMB was reflected in its effect of phase transformation, which was in the intermediate between 1,2,3-TMB and 1,3,5-TMB.

The phase transformation has been observed clearly from SEM (Figure S9) and HRTEM (Figure 8) images. Here, the detail observations were carried out in the synthesis system containing 1,2,3-TMB. As shown in Figure S9a, the sample T4 shows irregular monolithic shape which was proved to be two-dimensional hexagonal. Its HRTEM image exhibited a uniform hexagonal arrangement of bright dots corresponding to the straight channels. The diffraction pattern in the inset clearly shows that the incident beam is along the [001] direction.

It can be seen that the sample T10 consisted almost entirely of spherical particles, which grew into crystal with 54 and 74 faces gradually when the synthesis was conducted up to 24 h. We have already reported that the cubic phase having 54 and 74 crystal faces exhibits perfect HRTEM images characteristic of the cubic $Pm\bar{3}n$ space group.[14a] The HRTEM image for [100] and [111] incidences revealed regular periodicity over very large areas, and this clearly indicated that the particle is a single crystal with a well-ordered mesostructure. The sample T10 with spherical shapes proved to consist of perfect single crystals of the $Pm\bar{3}n$ space group as in the case of the particles having 54 and 74 crystal faces.[14a] HRTEM images projected along other incident beam directions [102], [112], and [110] also support the cubic $Pm\bar{3}n$ mesophase pore configuration (not shown).

The sample T5.5 comprised particles with two types of dominant morphologies as shown in Figure S9b. One of these had the form of the spheres that were observed in the sample T10, and the other exhibited the morphology of larger, irregular monoliths observed for the sample T4. It was estimated that the spheres and the monoliths corresponded to cubic and hexagonal mesophases, respectively. It can be even observed that the spherical shapes started to emerge on some monolith particles. These particular morphologies suggest that the one type of crystalline mesophase grew up on the other. The corresponding HRTEM image for [351], [321], and [210] also showed two types of distinct mesophase patterns. The one was the typical hexagonal *p*6*mm* array of the (10) plane, which was confirmed by tilting the specimen, and the other was the $Pm\bar{3}n$ cubic arrangement of the {211} plane. These corresponded to irregular and spherical parts of the particles observed in Figure S9a,c, respectively. Theses findings suggest that the {211} plane of the cubic phase was formed via the topological changes involving silica restructuring along the cylinder axis of the hexagonal phase. XRD patterns, SEM images, and HRTEM images showed that phase transformation proceeded with time from two-dimensional hexagonal to the cubic $Pm\bar{3}n$ phase through epitaxial growth of the cubic mesophase on the hexagonal mesophase.

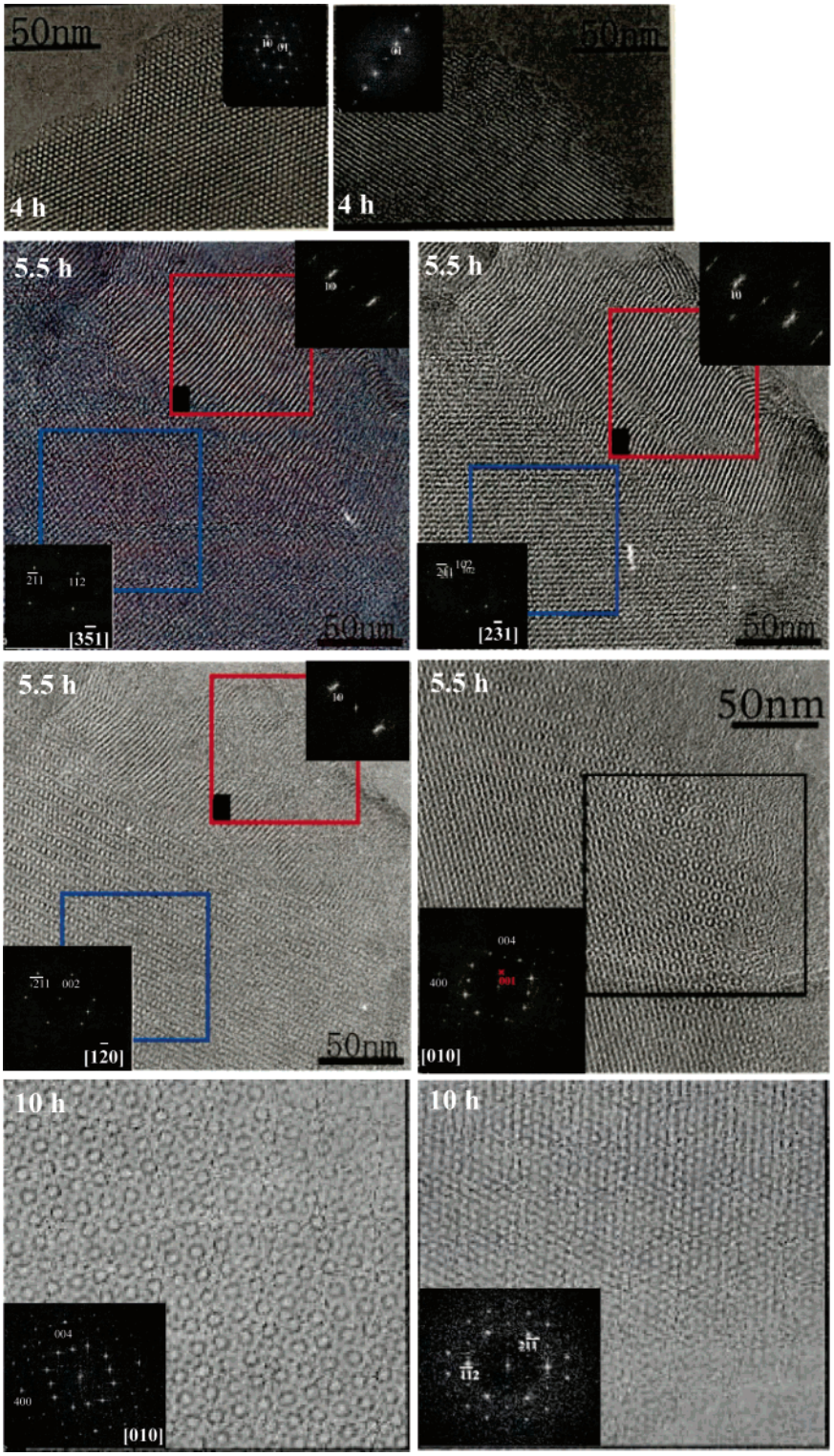

Figure 8. HRTEM images of the calcined materials synthesized with 1,2,3-TMB/CTEABr = 0.3 at 0 °C for various times.

2.2. Transformation from the Cubic $Pm\bar{3}n$ to the Three-Dimensional Hexagonal $P6_3/mmc$ Mesophase in the H_2SO_4 Synthesis System. Figure 9 shows an example of XRD patterns obtained with a composite synthesized in the three-dimensional hexagonal $P6_3/mmc$ mesostructure at an H_2SO_4/CTEABr molar ratio of 24.0. It is interesting to note that, in this system, the cubic $Pm\bar{3}n$ mesophase seemed to be formed first and converted to the three-dimensional hexagonal $P6_3/mmc$ mesophase gradually. At early times, it has been observed that the products had cubic $Pm\bar{3}n$ mesostructures, as indicated by the three peaks 200, 210, and 211 with d spacings of 42.84, 38.55, and 35.31, respectively. After 4 h three peaks of the cubic phase disappeared and were replaced by a set of more closed three peaks that could be indexed to 100, 002, and 101 reflections of the three-dimensional hexagonal $P6_3/mmc$ mesostructure. After 10 h, a highly ordered three-dimensional hexagonal mesostructure was formed.

The phase transformation can be clearly observed from SEM and HRTEM images. As shown in Figure 10, the

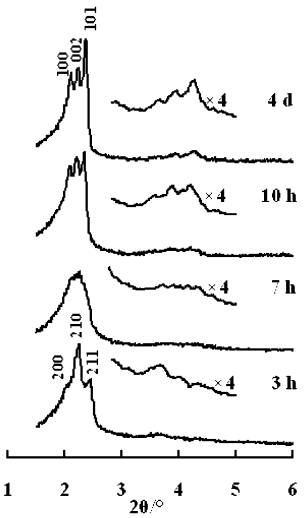

Figure 9. XRD patterns of as-synthesized materials synthesized under a H_2SO_4/CTEABr molar ratio of 24 for various times.

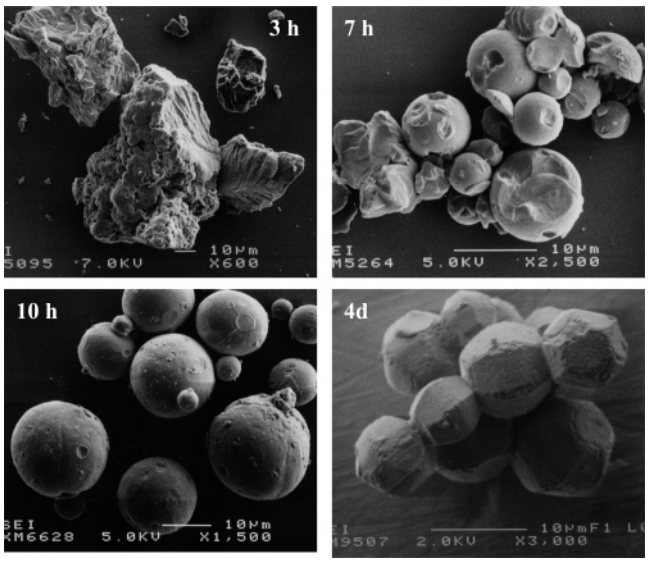

Figure 10. SEM images of the samples shown in Figure 9.

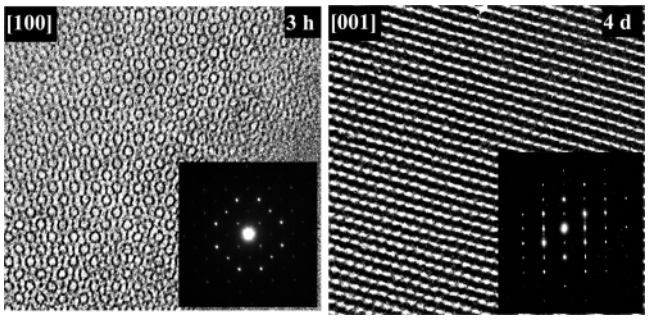

Figure 11. HRTEM images and their Fourier diffractograms of the samples shown in Figure 9.

material sampled at 3 h shows irregular particles which were assigned to the cubic $Pm\bar{3}n$ mesophase by HRTEM images (Figure 11). The diffraction pattern in the inset clearly shows that the incident beam directions [100] support the cubic $Pm\bar{3}n$ mesophase pore configuration.

It can be seen that the product sampled at 10 h consisted almost entirely of spherical particles, which grew into crystals with 20 faces gradually when the synthesis was conducted up to 4 days (Figure 10). We have mentioned above that the

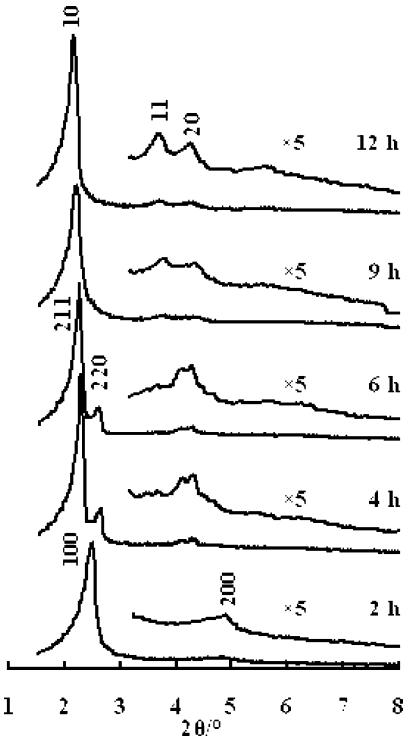

Figure 12. XRD patterns of as-synthesized materials synthesized with different acidities of HNO_3. Synthesis molar composition: 1:0.13:1:125 TEOS/CTEABr/HNO_3/H_2O.

three-dimensional hexagonal phase having 20 crystal faces exhibits perfect HRTEM images characteristic of the $P6_3/mmc$ space group. The HRTEM image (Figure 11) for [100] incidence revealed regular periodicity over very large areas, clearly indicating that the particle is a single crystal with a well-ordered mesostructure.

The sample synthesized for 7 h comprised particles with two types of dominant morphologies as shown in Figure 10. One of these had the form of spheres that were observed in the sample synthesized for 10 h, and the other exhibited the morphology of irregular particles observed for the sample synthesized for 3 h. It was estimated that the spheres and the irregular particles corresponded to three-dimensional hexagonal and cubic mesophases, respectively. XRD patterns, SEM images, and HRTEM images showed that phase transformation proceeded with time from cubic $Pm\bar{3}n$ to three-dimensional hexagonal. It has been reported that the g parameter of lyotropic liquid crystals of mesophases increases in the order cubic $Pm\bar{3}n$, three-dimensional hexagonal $P6_3/mmc$ < two-dimensional hexagonal $p6mm$ < cubic $Ia\bar{3}d$.[3d] Our results imply that the three-dimensional hexagonal $P6_3/mmc$ phase has a smaller g parameter than the cubic $Pm\bar{3}n$.

2.3. Mesophase Transformation Behavior of the HNO_3 Synthesis System. When HNO_3 was used as a counteranion source, a lamellar phase synthesized at early times was transformed to a two-dimensional hexagonal $p6mm$ mesophase through the cubic $Ia\bar{3}d$ mesophase. As shown in Figure 12, at the initial stage, the as-synthesized samples show a set of evenly spaced diffraction pattern peaks consistent with the lamellar structure. However, the peaks sharpened and increased in intensity with the time passed. They then gradually showed an increase in d spacing. The (100) and (200) peaks of the lamellar phase disappeared,

and many new peaks appeared simultaneously, which correspond to the cubic *Ia*$\bar{3}$*d* mesophase. Furthermore, the (211) peak of the cubic *Ia*$\bar{3}$*d* mesophase began to shift toward smaller 2θ values and the (220) peak disappeared. The three peaks (11), (20), and (21) corresponding to the two-dimensional hexagonal *p*6*mm* mesophase replaced the cubic peaks to grow in the 2θ range of 3−7°. The particles were gradually transformed from irregular to spiral or gyroid morphology (not shown).

Conclusions

The presence of various counteranions at the interfacial region of the silica−surfactant mesophase introduces opportunities for elaborate manipulation of the phase structure. Well-ordered mesoporous materials with a variety of mesostructures have been synthesized from the same silica source (TEOS) and surfactant (CTEABr) in H_2SO_4, HCl, HBr, and HNO_3 solutions, respectively. The counteranions of acidic media have resulted in increasing surface curvature of the mesophase in the order $SO_4^{2-} < Cl^- < Br^- < NO_3^-$, which leads to the formation of cubic *Pm*$\bar{3}$*n*, two-dimensional hexagonal *p*6*mm*, and lamellar mesophases initially with respect to acidity. Well-ordered three-dimensional hexagonal *P*6$_3$/*mmc*, cubic *Pm*$\bar{3}$*n*, two-dimensional hexagonal *p*6*mm*, and cubic *Ia*$\bar{3}$*d* mesoporous materials were formed via the transformation from cubic *Pm*$\bar{3}$*n*, two-dimensional hexagonal *p*6*mm*, lamellar or cubic *Ia*$\bar{3}$*d*, and lamellar, respectively. We have demonstrated the structural effect of TMB isomers on the rate of the mesophase transformation, indicating that 1,2,3-TMB was the most favored for the formation of the *p*6*mm* hexagonal mesophase, 1,3,5-TMB was the least, and 1,2,4-TMB showed intermediate behavior. In particular, the SEM and HRTEM images observation has presented visible evidence for the mesophase transformation, indicating that the phase transformation proceeded with time from the two-dimensional hexagonal to the cubic *Pm*$\bar{3}$*n* phase through epitaxial growth of the cubic mesophase on the hexagonal mesophase.

Acknowledgment. S.C. thanks Shanghai Jiao Tong University for financial support. This work was partially supported by Core Research for Evolutional Science and Technology (CREST) of JST Corporation and by the Swedish Research Council (VR).

Supporting Information Available: (1) Synthesis-space diagram of mesophase structures established by XRD measurements; (2) mesostructures synthesized with different synthesis compositions; (3) SEM images and surface indexes of three-dimensional hexagonal *P*6$_3$/*mmc* and *Pm*$\bar{3}$*n* mesoporous silica synthesized with H_2SO_4 and HCl, respectively; (4) HRTEM images and Fourier diffractograms of the three-dimensional hexagonal *P*6$_3$/*mmc* mesophase synthesized with H_2SO_4; (5) N_2 adsorption−desorption isotherms and pore size distributions of calcined mesoporous materials synthesized with different acids; (6) XRD patterns of as-synthesized materials synthesized by the addition of 1,2,4-TMB at 0 °C for various times; (7) XRD patterns of as-synthesized materials synthesized by the addition of 1,2,3-TMB at 0 °C for various times; (8) Si/CTEABr molar ratio of as-synthesized materials synthesized by the addition of 1,2,3-TMB at 0 °C for various times; (9) SEM images of as-synthesized materials synthesized with 1,2,3-TMB addition at 0 °C for various times; (10) properties of the four types mesoporous materials (pdf). This material is available free of charge via the Internet at http://pubs.acs.org.

CM050359S